Journal of Petroleum Science and Engineering 112 (2013) 61–68

Contents lists available at ScienceDirect

Journal of Petroleum Science and Engineering

journal homepage: www.elsevier.com/locate/petrol

A 3D compositional miscible gas flooding simulator with dispersion using Element-based Finite-Volume method

Luiz Otávio Schmall dos Santos [a], Francisco Marcondes [b], Kamy Sepehrnoori [a,*]

[a] Petroleum and Geosystems Engineering Department, The University of Texas at Austin, 1 University Station C0300, Austin, TX 78712-0228, USA
[b] Department of Metallurgical Engineering and Material Science, Federal University of Ceará, Fortaleza, Ceará, Brazil

ARTICLE INFO

Article history:
Received 16 February 2013
Accepted 2 October 2013
Available online 6 November 2013

Keywords:
physical dispersion
compositional reservoir simulation
unstructured meshes
EbFVM

ABSTRACT

Physical dispersion is one of the most important key parameters in compositional reservoir simulation. It is a phenomenon of mixing with mass transfer occurring when gradients in composition arise or exist. This process tends to homogenize the composition of the phases. When the dispersion term is included in the material balance equations, we obtain a full tensor structure. However, most of the reservoir simulators neglect such an important physical term. In this work, we investigate the governing partial differential equations for modeling miscible flooding by adding dispersion to the material balance equations. The equations are solved by the Element-based Finite-Volume method (EbFVM) in conjunction with unstructured meshes. Results of several compositional reservoir simulation case studies are presented to demonstrate the application of the method.

1. Introduction

Gas injection is one of the most important methods for enhanced oil recovery; but requires careful and prudent modeling in order to correctly predict field production (Corrêa et al., 1990; Lim et al., 1997). One of the key physical parameters associated with miscible gas displacement is physical dispersion. In the cases of miscible and immiscible gas injections, surfactant flooding, and tracer injection, physical dispersion plays an important role because it has a direct influence on the mixing process. As verified by Yanze and Clemens (2012) and Paraschiv et al. (2012), physical dispersion has a direct impact in fractured reservoir simulation. According to these authors, neglect of dispersion can result in large errors in oil recovery compared to the case including physical dispersion. Although the importance of physical dispersion has been known in miscible gas process, most commercial simulators do not take into account this term in the recovery process (Oldenburg et al., 2001; Costanza-Robinson and Brusseau, 2006). This is mainly due to the nature of the full dispersion tensor that gives rise to approximate equations whose Jacobian matrix stencil is much larger than the one we obtain when the dispersion term is not included in a fully implicit compositional simulator. According to Arya et al. (1988), dispersion mixing is caused by variations (heterogeneity) in the velocity within each flow channel and from one channel to another. Molecular diffusion is the transport of mass because of spatial concentration differences. Dispersion and diffusion in permeable media play an important role in miscible displacement, where channeling and/or fingering of the displacing fluid occurs. As described by Maliska (2004), one of the problems arising in the solution of advection–diffusion problem is the numerical dispersion caused by inexact interpolation functions. This numerical dispersion can be amplified in simulation cases due to the grid orientation effects. Several approaches have been used to minimize the numerical dispersion during modeling of physical dispersion. Arya et al. (1988) using Cartesian meshes suggest decreasing the mesh size in order to reduce the numerical dispersion and then extrapolating the results to zero block size. Corrêa et al. (1990) solved the equations arising from the dispersion modeling by inverting the solution from Laplace space to time space using a numerical inversion. Oldenburg et al. (2001) used numerical dispersion to mimic the physical dispersion when they investigated CO_2 injection into natural gas reservoirs. Lim et al. (1997) investigated the effect of numerical dispersion in miscible gas recovery through grid refinement and use of upwind and third order TVD schemes. Marcondes and Sepehrnoori (2010) and Marcondes et al. (submitted for publication) demonstrated that use of unstructured meshes in conjunction with EbFVM can reduce the number of gridblocks required to obtain mesh-independent solutions for gas injection processes, respectively for 2D and 3D reservoirs. We expect that the EbFVM approach can be more accurate than the convectional Cartesian grids associated with physical dispersion.

Several authors highlighted the importance of appropriate modeling of physical dispersion (Stalkup, 1990; Haajizadeh et al.,

* Corresponding author. Tel./fax: +1 512 417 0231.
E-mail address: kamys@mail.utexas.edu (K. Sepehrnoori).

0920-4105/$ - see front matter © 2013 Elsevier B.V. All rights reserved.
http://dx.doi.org/10.1016/j.petrol.2013.10.004

1999; Solano et al., 2001; Shrivastava et al., 2002) in miscible gas processes. In order to incorporate the effects of physical dispersion, few researchers have tried to find a grid block size whose numerical dispersion mimics the physical dispersion (Haajizadeh et al., 1999). The main idea of this approach is to explore the inherent numerical dispersion in the finite difference method to find a grid block size capable of accurately representing the mass transfer transport with physical dispersion. As pointed out by Fanchi (1983), this methodology is difficult to apply to real field cases and can lead to errors in one or more cross flow directions.

Chang (1990) presented a method to incorporate physical dispersion in an IMPEC compositional reservoir simulator. Later Chang et al. (1994) investigated the formation of viscous fingering for different dispersivity scenarios of CO_2 injection. Shrivastava et al. (2005a, 2005b) presented a similar approach as proposed by Chang et al. (1994) to incorporate physical dispersion in a fully implicit compositional reservoir simulator.

In this study, we introduce a similar methodology as proposed by Chang (1990) in a fully implicit compositional reservoir simulator based on Coats (1980) formulation for Cartesian grids. The original formulation of Coats (1980) is implemented using an Element-based Finite-Volume Method (EbFVM) as described in Marcondes and Sepehrnoori (2007, 2010). This approach has been implemented for several gas flooding reservoir simulation studies and has been shown to be less prone to the numerical dispersion effect. In this approach, we expect that the correct effect of the physical dispersion can be correctly modeled through simulation.

We implemented the EbFVM in conjunction with the physical dispersion in an in-house simulator called General purpose Adaptive Simulator (GPAS). The current implementation adds a new capability, by adding the dispersion term in the simulator, compared with the previous EbFVM implementations carried out in GPAS. GPAS was developed at the Center for Petroleum and Geosystems Engineering at The University of Texas at Austin for the simulation of enhanced recovery processes. GPAS is a fully implicit, multiphase/multi-component simulator, which can handle simulation of several enhanced oil recovery processes. This simulator is divided into two main modules: Framework and EOScomp. Framework is responsible for input/output and memory allocation, while EOScomp handles the computations for flash calculation and solution of non-linear equations arising from the discretization of the governing equations. Details for EOScomp and Framework modules can be found in Wang et al. (1997) and Parashar et al. (1997), respectively.

2. Physical model

The mathematical problem for compositional modeling is composed of $(n_p-1)n_c+n_p+1$ equations (where n_c is the number of components and n_p is the number of phases present in the system) which give rise to $(n_p-1)n_c+n_p+1$ unknowns as follows.

For each component i there is one material balance equation defined by

$$\frac{\partial}{\partial t}(\phi N_i)-\vec{\nabla}\cdot\sum_{j=2}^{n_p}(\xi_j x_{ij}\lambda_j\overline{\overline{K}}\cdot\nabla\Phi_j-\phi\xi_j S_j\overline{\overline{K}}_{ij}\cdot\nabla x_{ij})-q_i=0, \tag{1}$$

where ϕ is the porosity of the control volume, $\overline{K}$ is the full and symmetric absolute permeability tensor, λ_j, μ_j, and ξ_j are the mobility, the viscosity, and the density of the j-th phase, respectively, Φ_j is the potential of the phase j, S_j is the saturation of the phase j, $\overline{\overline{K}}_{ij}$ is the full dispersion tensor for the component i at the phase j, x_{ij} is the mole fraction of the component i at the phase j, q_i is the molar flow rate of the component i due to well injection/production per unit of bulk volume. The number of moles of component i per pore volume (N_i) and the phase potential are defined by

$$N_i=\sum_{j=2}^{n_p}\xi_j S_j x_{ij}, \tag{2}$$

$$\Phi_j=P_j-\gamma_j D, \tag{3}$$

where γ_j is the specific weight of phase j, D is the depth, which is positive in the downward direction.

The second term inside the parenthesis in Eq. (1) is the mass transport by diffusion/dispersion. For this term, the full symmetric dispersion tensor $\overline{\overline{K}}_{ij}$ is given by

$$\overline{\overline{K}}_{ij}=\begin{pmatrix}K_{xx} & K_{xy} & K_{xz}\\ K_{xy} & K_{yy} & K_{yz}\\ K_{xz} & K_{yz} & K_{zz}\end{pmatrix}_{ij}, \tag{4}$$

which can be expanded by (Lake, 1989)

$$K_{xx}=\frac{D_{ij}}{\tau}+\frac{\alpha_{lj}}{\phi S_j}\frac{u_{xj}^2}{|u_j|}+\frac{\alpha_{tj}}{\phi S_j}\frac{u_{yj}^2}{|u_j|}+\frac{\alpha_{tj}}{\phi S_j}\frac{u_{zj}^2}{|u_j|}, \tag{5a}$$

$$K_{yy}=\frac{D_{ij}}{\tau}+\frac{\alpha_{lj}}{\phi S_j}\frac{u_{yj}^2}{|u_j|}+\frac{\alpha_{tj}}{\phi S_j}\frac{u_{xj}^2}{|u_j|}+\frac{\alpha_{tj}}{\phi S_j}\frac{u_{zj}^2}{|u_j|}, \tag{5b}$$

$$K_{zz}=\frac{D_{ij}}{\tau}+\frac{\alpha_{lj}}{\phi S_j}\frac{u_{zj}^2}{|u_j|}+\frac{\alpha_{tj}}{\phi S_j}\frac{u_{xj}^2}{|u_j|}+\frac{\alpha_{tj}}{\phi S_j}\frac{u_{yj}^2}{|u_j|}, \tag{5c}$$

$$K_{xy}=\frac{\alpha_{lj}-\alpha_{tj}}{\phi S_j}\frac{u_{xj}u_{yj}}{|u_j|}, \tag{5d}$$

$$K_{xz}=\frac{\alpha_{lj}-\alpha_{tj}}{\phi S_j}\frac{u_{xj}u_{zj}}{|u_j|}. \tag{5e}$$

In Eqs. (5a)–(5e), we can see a new parameter, α, which Bear (1988) defined as the medium's (geometrical) dispersivity. According to Lake (1989), this parameter depends on rock properties and also by the scale of the experiment. Finally, u_j is the phase velocity and is given by Darcy's equation.

For the water phase, there is an additional material balance equation which is given by

$$\frac{\partial}{\partial t}(\phi N_w)-\vec{\nabla}\lambda_w\xi_w\cdot\overline{\overline{K}}\cdot\nabla\Phi_w-q_w=0, \tag{6}$$

where the subscript w refers to the water phase. It is important to mention that there is no mass transfer between hydrocarbon components and water. Therefore, no physical dispersion was added to the water molar balance equation.

For each component there are $n_c(n_p-2)$ fugacity constraints as follows:

$$f_i^2-f_i^j=0 \quad \text{for} \quad j=3\cdots n_p \quad \text{and} \quad i=1,\ldots,n_c, \tag{7}$$

where f_i^j is the fugacity of component i in phase j. It is worthwhile to mention that in Eq. (7), the fugacity of the oil phase (2) was selected as the base for the fugacity calculation of all other phases when three or more hydrocarbon phases are present.

There are also n_p-1 mole fraction constraints:

$$\sum_{i=1}^{n_c}x_{ij}=1 \quad \text{for } j=2\cdots n_p. \tag{8}$$

Finally, there is one volume constraint defined by

$$\sum_{j=1}^{n_p}\frac{N_j}{\xi_j}-1=0 \quad \text{or} \quad \sum_{j=1}^{n_p}S_j-1=0. \tag{9}$$

3. Approximate equations

In this work, the approximate equations are obtained by using the EbFVM. In the EbFVM, each element is divided into sub-elements. The conservation equations, Eqs. (1) and (6), need to be integrated for each of these sub-control volumes. We have employed for the numerical discretization four element types (hexahedron, tetrahedron, prism and pyramids) which allows the use of hybrid meshes. Fig. 1 presents the four element types. Integrating each term of Eq. (1) in time and for each of the sub-control volumes and applying the Gauss theorem for the advective and dispersion terms we obtain:

$$\int_{V,t}\frac{\partial}{\partial t}(\phi N_i)dV\,dt-\int_{V,t}\sum_{j=2}^{n_p}(\lambda_j\xi_j x_{ij}\overline{\overline{K}}\cdot\nabla\Phi_j-\phi\xi_j S_j\overline{\overline{K}}_{ij}\cdot\nabla x_{ij})\cdot\overrightarrow{dA}\,dt-\int_{V,t}q_i dV\,dt=0. \tag{10}$$

In order to evaluate the accumulation and the advective and dispersion terms of Eq. (10) for each of the four element types, we used the shape functions defined in Marcondes et al. (submitted for publication). The shape functions allow calculation of the position vector and the physical properties inside each element from the latter known for the vertices of each element. In the EbFVM approach we used, it is assumed that each element has a constant permeability tensor. Hence, when the advective fluxes are evaluated at each interface of each sub-control volume no interpolation function is necessary. It should be emphasized that if a block-centered approach was used instead of a cell-vertex approach, some interpolation for the permeability tensor would be necessary; for instance, the one used by multipoint flux approximation (Verma and Aziz, 1997; Edwards, 2000; Edwards, 2002). We should emphasize that in the second option, the control volume around each vertex will have constant porosity and absolute permeability tensor. For the dispersion tensor components, as there is phase dependency through the phase velocity we evaluate for the velocity of each phase at each integration point using the shape functions of each element. This approach allows a complete variation through the element of the physical dispersion tensor. Performing the integration of first and second terms of Eq. (10) and evaluating the fluid properties through a fully implicit procedure, the following equations for the two mentioned terms are obtained:

$$Acc_{m,i}=Vscv_{m,i}\left(\left(\frac{\phi N_m}{\Delta t}\right)_i-\left(\frac{\phi N_m}{\Delta t}\right)_i^o\right);\quad m=1,\,N_v;\quad i=1,..,\,n_c, \tag{11}$$

$$F_{m,i}=\int_A\sum_{j=1}^{n_p}(\lambda_j\xi_j x_{ij}\overline{\overline{K}}\cdot\nabla\Phi_j-\phi\xi_j S_j\overline{\overline{K}}_{ij}\cdot\nabla x_{ij})\cdot\overrightarrow{dA}=\int_A\left(\sum_{j=1}^{n_p}\xi_j x_{ij}\lambda_j K_{nl}\frac{\partial\Phi_j}{\partial x_l}-\phi\xi_j S_j K_{ijnl}\frac{\partial x_{ij}}{\partial x_l}\right)dA_n;$$
$$m=1,\,N_e;\quad n,l=1,\,3. \tag{12}$$

In the above equations N_v and N_e denote the number of vertices and the number of elements of the grid, respectively. By inspecting Eq. (12), it can be inferred that it is necessary to evaluate molar densities, molar fraction, and mobilities for each interface of each sub-control volume. To evaluate these properties, an upwind scheme based on Cordazzo et al. (2004) will be used. Mobilities and other fluid properties are evaluated at the integration point 1 in Fig. 1a, for instance by

$$\lambda_{j1}=\lambda_{j2}\quad\text{if}\quad\overline{K}\cdot\nabla\Phi_j\cdot\overrightarrow{dA}\Big|_{ip1}\le 0$$

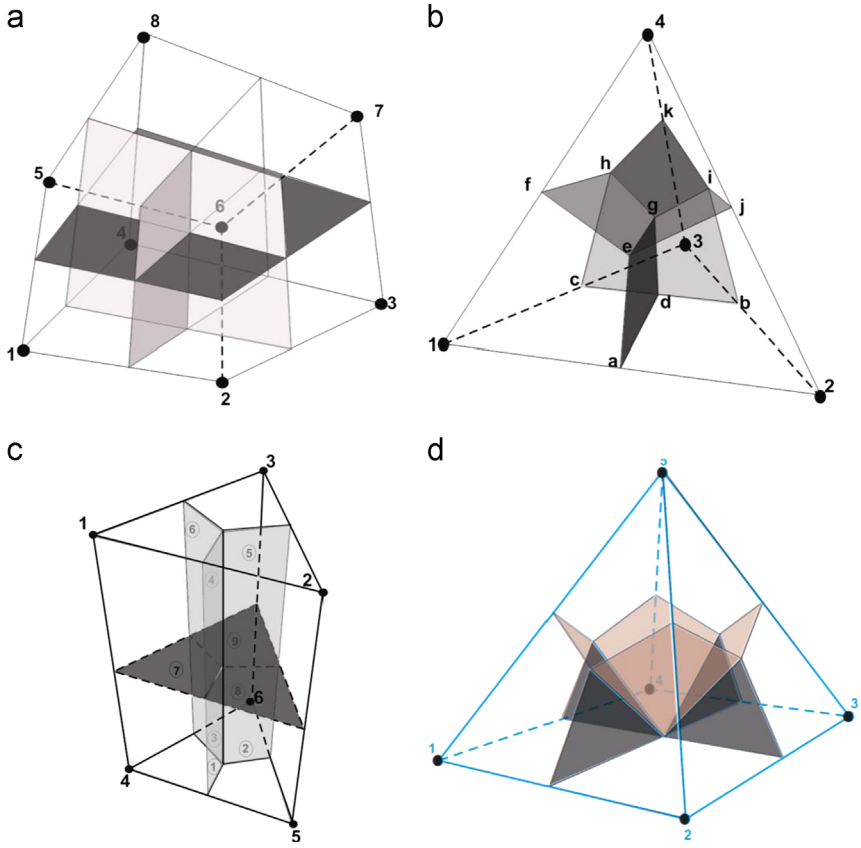

Fig. 1. 3D elements and their respective sub-control volumes. (a) Hexahedron, (b) tetrahedron, (c) prism and (d) pyramid.

$$\lambda_{j1} = \lambda_{j1} \quad \text{if} \quad \overline{K} \cdot \nabla \Phi_j \cdot \overrightarrow{dA}\Big|_{ip1} > 0 \tag{13}$$

Inserting Eqs. (11) and (12) into (10), the following equation for each element is obtained:

$$Acc_{m,i} + F_{m,i} + q_i = 0; \quad m = 1,\ N_e; \quad i = 1,\ n_c + 1 \tag{14}$$

Eq. (14) denotes the conservation for each sub-control volume of each element. Now, it is necessary to assemble the equation of each control volume for obtaining the contribution of each sub-control volume that shares the same vertex. This process is similar to assembling of the stiffness global matrix in the finite element method. Further details can be found in Cordazzo et al. (2004) and Marcondes and Sepehrnoori (2007, 2010). Finalizing this section, it is important to mention that each element can have different permeabilities and porosities, allowing simulation of high anisotropic reservoirs.

4. Test problems

This section presents four simulation case studies for investigation of the dispersion tensor effect in conjunction with the EbFVM approach. The first case study refers to simulation of tracer injection into a one-dimensional isotropic and homogeneous reservoir saturated with water. Table 1 presents the fluid and physical properties.

The second case study refers to a two-dimensional simulation in a quarter-of-five spot of tracer injection in a homogeneous and isotropic saturated reservoir. The fluid and physical properties are presented in Table 2.

The third case study refers to solvent injection in a quarter-of-five spot, but now a heterogeneous reservoir has been considered and a 3D variation of fluid and rock properties has been taken into account. Tables 3 and 4 present the fluid and physical properties and Corey's model coefficients (Eq. (15)), respectively. The K_{xx} absolute permeability of the field is shown in Fig. 2. For each grid block, the same value of K_{xx} was used for K_{yy}, and the value of K_{zz} was set to one-tenth of the K_{xx} component. The other components of the absolute permeability tensor were set to zero.

$$K_{rj} = K_{rj}^0 S_j^{n_j}; \quad \overline{S}_j = \frac{S_j - S_j^0}{1 - \sum_{i=1}^{np} S_i^0} \tag{15}$$

where S_j^0 denotes the residual saturation of the j-th phase, and the others parameters were previously defined in Table 4.

The last case study refers to simulation of solvent injection into an irregular reservoir. Except for the reservoir dimensions and the absolute permeabilities, we used the same properties shown in Tables 3 and 4. Fig. 3 shows two grid-configurations employed for this reservoir. The first mesh, Fig. 3a, is composed only of hexahedrons, while the other one, Fig. 3b, is a hybrid mesh composed of tetrahedron, pyramid and hexahedron elements. In Fig. 3a and b, we show the reservoir top and bottom topologies, respectively. From these figures, we can see that this reservoir is irregular in the x, y, and z directions. The absolute permeabilities in the x and y directions are 5.0×10^{-13} m^2 (500 mD), and the absolute permeability in the z direction is 5.0×10^{-14} m^2 (50 mD). For each injection well, we used the volumetric rate presented in Table 3.

Table 1
Input data for Case 1.

Reservoir data	Initial conditions	Physical properties and well conditions
Reservoir dimension (L_x=12.192 m, L_z=L_y=0.03048 m) Absolute permeability (K_{xx})=5.0×10^{-13} m^2 (500 mD) Porosity=0.2 Peclet number (N_{pe})=200	Water saturation S_{wi}=1.0 Reservoir pressure=13.79 MPa (2000 psi)	Water viscosity=2.49×10^{-4} Pa s Water density=87.70 mol/m^3 (2.4833 lbmol/ft^3) Bottom hole pressure=13.79 MPa (2000 psi) Injected well rate=1.31×10^{-8} m^3/s (7.13×10^{-3} barrels/day) Tracer concentration=1.0

Table 2
Input data for Case 2.

Reservoir data	Initial conditions	Physical properties and well conditions
Reservoir dimension (L_x=L_y=502.92 m, L_z=0.3048 m) Absolute permeability (K_{xx}=K_{yy}=K_{zz})=5.0×10^{-13} m^2 (500 mD) Porosity=0.2 Longitudinal dispersivity (α_l)=2.01 m Transversal dispersivity (α_t)=0.201 m	Water saturation S_{wi}=1.0 Reservoir pressure=0.689 MPa (100 psi)	Water viscosity=0.249×10^{-3} Pa s Water density=87.70 mol/m^3 (2.4833 lbmol/ft^3) Bottom hole pressure=0.689 MPa (100 psi) Injected well rate=5.12×10^{-3} m^3/s (2785 barrels/day) Tracer concentration=1.0

Table 3
Input data for Case 3.

Reservoir data	Initial conditions	Physical properties and well conditions
Reservoir dimension (L_x=L_y=609.6 m, L_z=60.96 m) Porosity=0.30 Longitudinal dispersivity (α_l)=2.01 m Transversal dispersivity (α_t)=0.201 m	Water saturation S_{wi}=0.25 Reservoir pressure=13.79 MPa (2000 psi) Overall fraction of hydrocarbon components (CO_2, C_1, C_3, C_6, C_{10}, C_{15}, C_{20})=0.01, 0.20, 0.30, 0.05, 0.025, 0.025, 0.39	Water viscosity=1×10^{-3} Pa s Gas injection rate=3.28 m^3/s (10^7 ft^3/d) Bottom hole pressure=13.10 MPa (1900 psi) Injected mole fraction (CO_2, C_1, C_3, C_6, C_{10}, C_{15}, C_{20})=0.7, 0.2, 0.065, 0.02, 0.01, 0.004, 0.001

5. Results

Fig. 4 presents results of the dimensionless concentration of tracer versus the dimensionless length of the reservoir for case 1. The results of this simulation using the GPAS simulator in conjunction with Cartesian grid are also shown and both are compared with the analytical. Fig. 4 shows that the results of the present work using a Hexahedron element (500 elements; 2004 vertices) and the Cartesian (1000 grid blocks) mesh match the analytical solution. As the control-volumes are created around each vertex of the mesh, it is important to mention that the number of vertices of the EbFVM approach is equal to the number of control volumes. Also, a 3D formulation is used to run this case. Therefore, in terms of discretization of the problem, we have 501 control volumes in the flux direction. Thus, we can verify that the number of control volumes of the coarse Cartesian mesh is about twice larger than the hexahedron grid.

The results in terms of normalized effluent tracer concentration obtained for Case 2 are shown in Fig. 5. Fig. 5 compares several hexahedron grids in conjunction with the EbFVM approach and Cartesian meshes and the analytical solution. From this comparison, we can see that a good match for the

Table 4
Corey's model relative permeability data for Case 3.

Relative permeability parameters	Water	Oil	Gas	Second oil
End point relative permeability	0.3	0.75	0.9	0.9
Residual saturation	0.25	0.2	0.0	0.0
Exponent of relative permeability	2.0	2.0	2.0	2.0

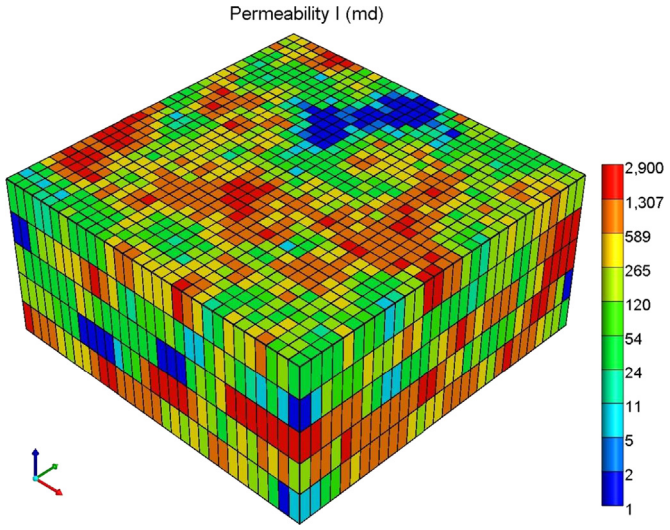

Fig. 2. Component of K_{xx} absolute permeability field – Case 3.

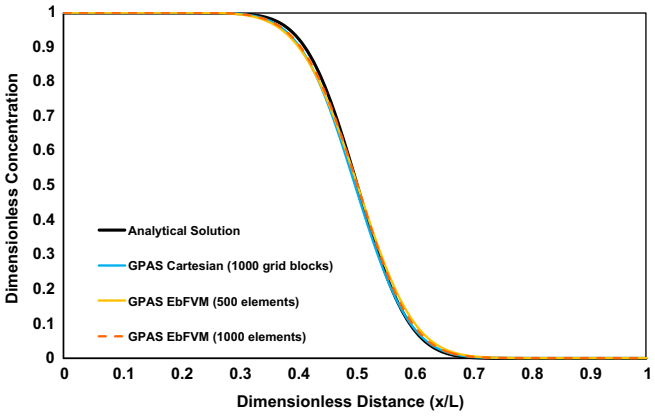

Fig. 4. Dimensionless concentration at 0.5 pore volume – Case 1.

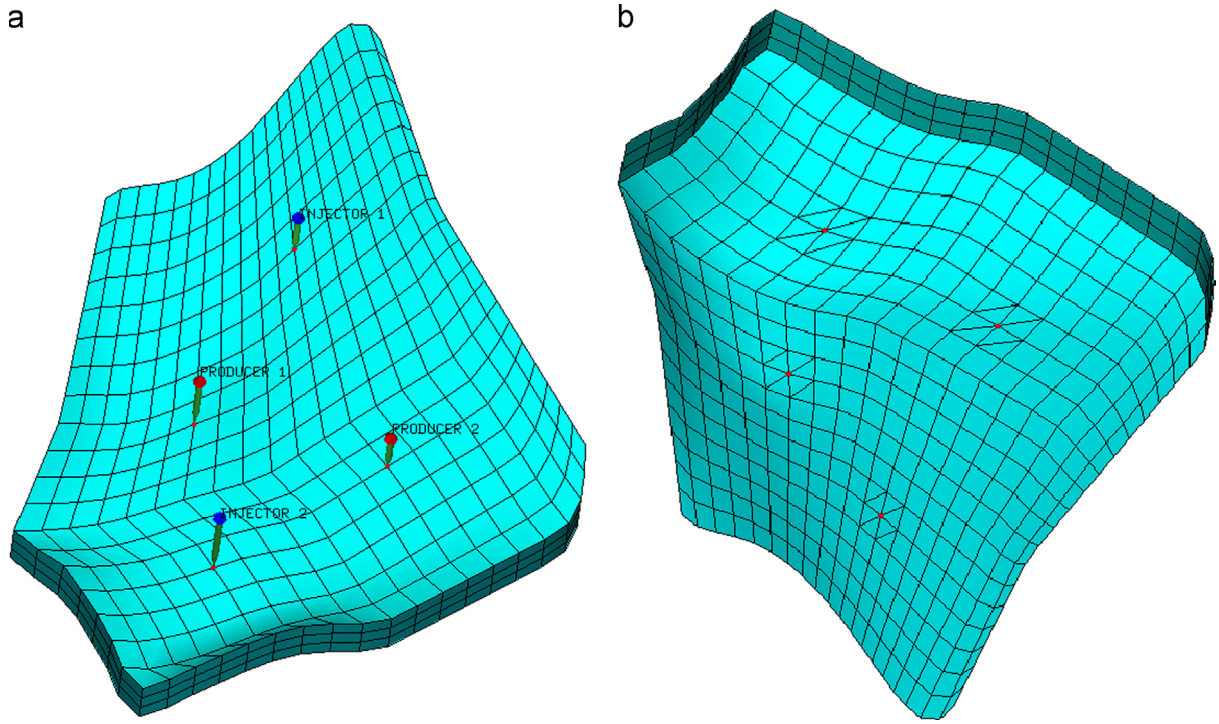

Fig. 3. Reservoir and grid-configurations used for Case 4. (a) Top view and (b) bottom view.

breakthrough time was obtained with the "$100 \times 100 \times 1$" EbFVM mesh, but the same was not true for the same level of refinement of the Cartesian mesh. Also, we can observe that for all the three levels of grid refinement investigated (30×30, 50×50, and 100×100), the EbFVM approach always produced concentration curves with less numerical dispersion compared to the original GPAS approach using Cartesian grids. In order to test the capability of the EBFVM approach for reducing the numerical dispersion, it is also important to mention that an upwind scheme was used for both formulations (EbFVM and Cartesian).

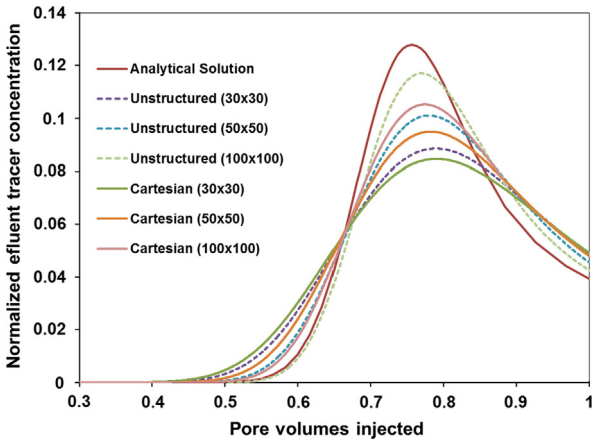

Fig. 5. Normalized effluent tracer concentration versus pore volumes injected.

The results for Case 3, in terms of volumetric rates at standard conditions of oil and gas, obtained in conjunction with hexahedron element and Cartesian grid are shown in Fig. 6. From Fig. 6, we can observe that the volumetric rates by the hexahedron mesh are close to the ones obtained by the Cartesian mesh. Spikes present in the curves are due to phase changes in the reservoir associated with the phase composition and pressure changes. We also would like to stress that because the EbFVM approach has a larger stencil than the Cartesian grid, we expect to see more spikes in the volumetric rates than observed for both oil and gas production rates. Comparing both curves, we can see that the breakthrough in the EbFVM mesh was later than in the Cartesian one. Fig. 7 presents CO_2 concentration fields at 2500 days for both EbFVM and Cartesian grids. From this figure, we can see that although the fronts are similar, the EbFVM mesh presents sharper fronts, since the numerical dispersion is lower for this approach.

Fig. 8 presents the results, in terms of oil and gas volumetric rates at standard condition, for the last case study in conjunction with the two meshes shown in Fig. 3. Although the two grid configurations are different, the results in terms of oil and gas rates for both grids are in good agreement. The CO_2 mole fraction for two simulation times is shown in Fig. 9 for the two grid configurations. From this figure, it can be seen that a reasonable agreement between results using two different grid configurations has been obtained.

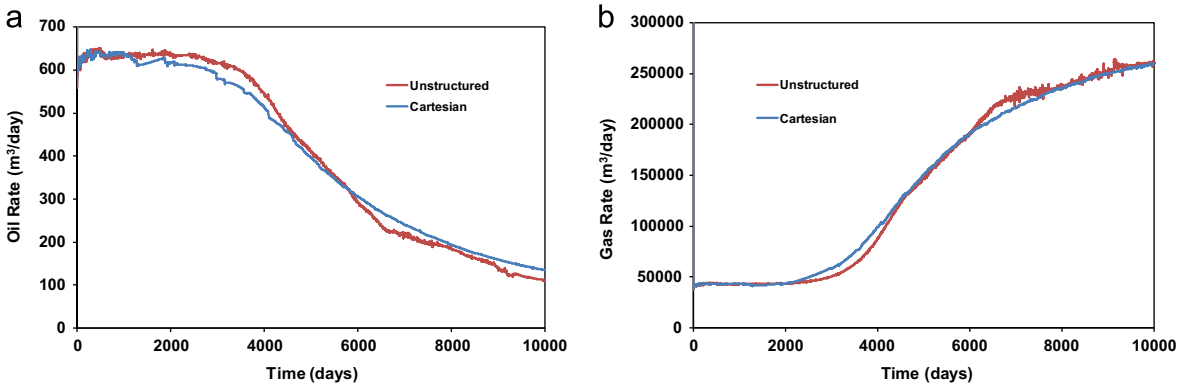

Fig. 6. Results for Case 3. (a) Oil production rate versus time and (b) gas production rate versus time.

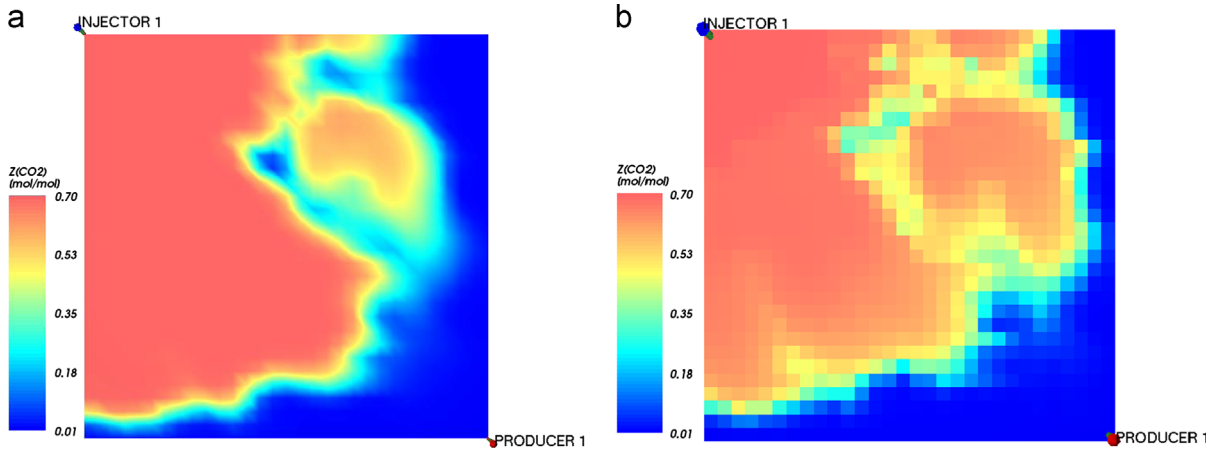

Fig. 7. Results for Case 3. (a) EbFVM CO_2 mole fraction at 2500 days and (b) Cartesian CO_2 mole fraction at 2500 days.

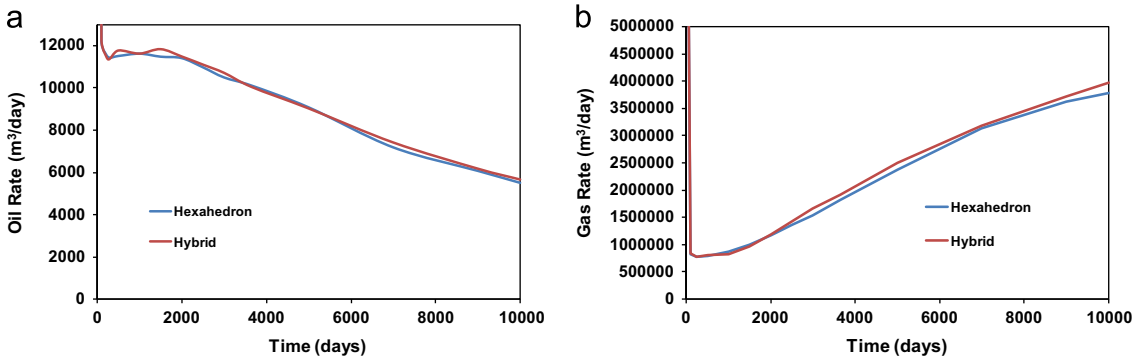

Fig. 8. Results for Case 4. (a) Oil production rate versus time and (b) gas production rate versus time.

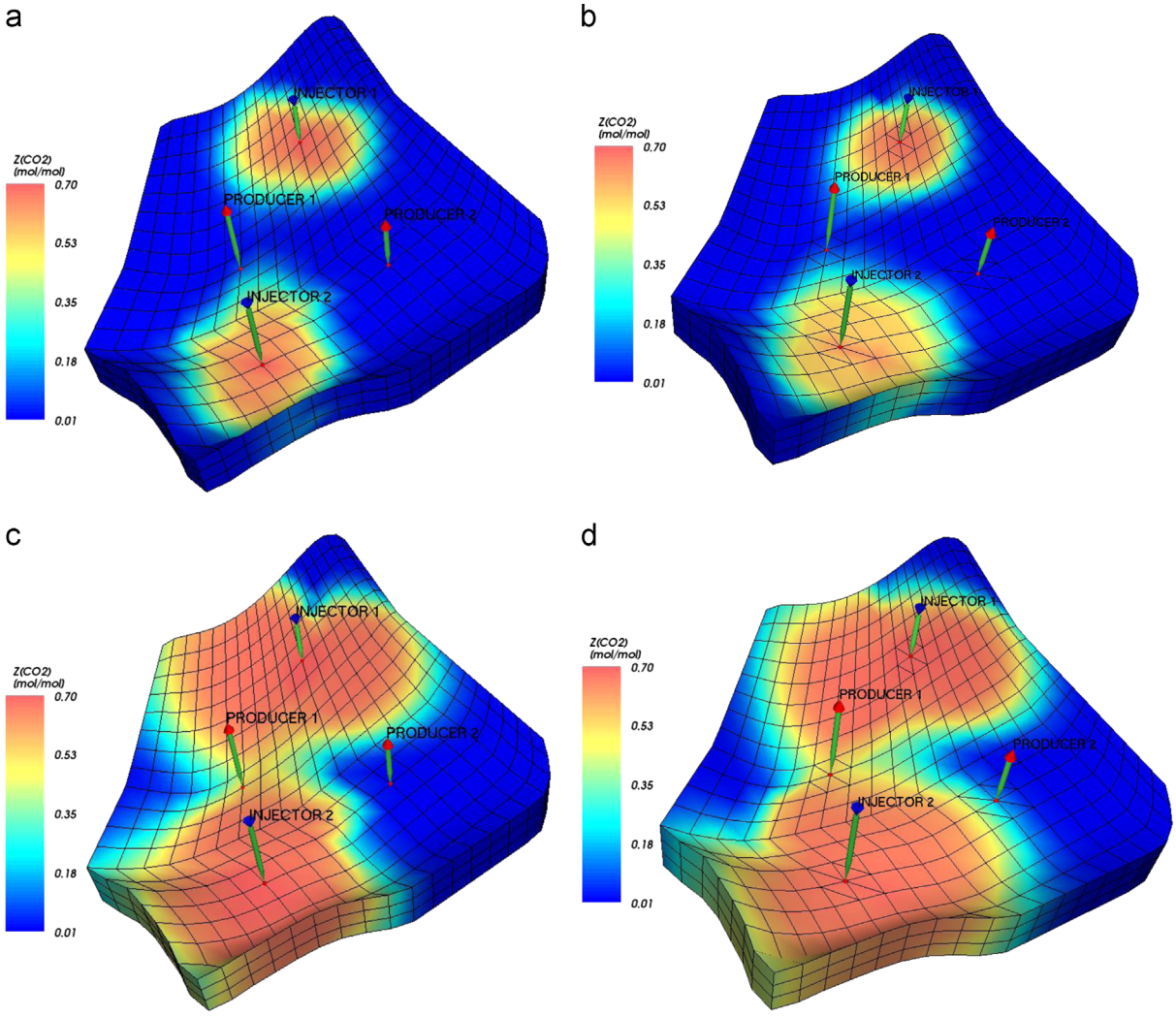

Fig. 9. CO_2 mole fraction field – Case study 4. Hexahedron: (a) 1500 days and (b) 7000 days. Hybrid: (c) 1500 days and (d) 7000 days.

6. Conclusions

Physical dispersion full tensor was implemented in an in-house compositional simulator in conjunction with an element-based finite volume approach using unstructured grids. The methodology was tested for four different case studies: two tracer injections (1D and 2D), and two case studies involving solvent injection. The results of 1D tracer injection were compared to the analytical solution and to the results of GPAS in conjunction with Cartesian meshes. The results suggest that the element-based approach reduces numerical dispersion, compared to the Cartesian meshes. The results of the second case study (2D tracer injection) are also demonstrated to be more accurate than the ones using Cartesian meshes. The two other applications were performed in a heterogeneous quarter-of-five-spot and in a reservoir with a complex geometry. The results demonstrate the flexibility of the method in representing complex reservoirs and difficult phase behavior and also its capacity to deal with heterogeneous media. In conclusion,

the EbFVM approach was tested for several case studies involving physical dispersion. Based on the results, the approach presented advantages, compared to the traditional Cartesian meshes.

Acknowledgments

This work was conducted with the support of the Reservoir Simulation Joint Industry Project, a consortium of operating and service companies at the Center for Petroleum and Geosystems Engineering at The University of Texas at Austin. Also, the first author would like to thank Petrobras (Petróleo Brasileiro S.A.) for his financial support. Finally, the second author likes to thank CNPq (The National Council for Scientific and Technological Development of Brazil) for their support through the grant 305415/2012-3.

References

Arya, A., Hewett, T.A., Larson, R.G., Lake, L.W., 1988. Dispersion and reservoir heterogeneity. SPE Reserv. Eng. 3, 139–148.

Bear, J., 1988. Dynamics of Fluids in Porous Media, Dover publications, New York.

Chang, Y.B., 1990. Development and Application of an Equation-of-State Compositional Simulator. (Ph.D. dissertation). The University of Texas at Austin.

Chang, Y.B., Lim, M., Pope, G., Sepehrnoori, K., 1994. CO_2 flow patterns under multiphase flow: heterogeneous field-scale conditions. SPE Reserv. Eng. 9 (3), 208–216.

Costanza-robinson, M.S., Brusseau., M.L., 2006. Gas-phase dispersion in porous media. In: Ho, C., Webb, S. (Eds.), Gas Transport in Porous Media. Springer, Dordrecht, The Netherlands, pp. 121–132.

Coats, K.H., 1980. An equation of state compositional model. SPE Paper 8284. SPE J. 20 (5), 363–376.

Cordazzo, J.,Maliska, C. R., Silva, A.F.C., Hurtado, F.S.V., 2004. The negative transmissibility issue when using CVFEM in petroleum reservoir simulation—1. Theory. In: Proceedings of the 10th Brazilian Congress of Thermal Sciences and Engineering — ENCIT 2004, November 29 – December 03. Brazilian Society of Mechanical Sciences and Engineering — ABCM, Rio de Janeiro, Brazil.

Corrêa, A.C., Pandle, K.K., Ramey Jr., H.J., Brigham, W.E., 1990. Computation and interpretation of miscible displacement performance in heterogeneous porous media. SPE Reserv. Eng. 5, 69–78.

Edwards, M.G., 2000. M-matrix flux splitting for general full tensor discretization operators on structured and unstructured grids. J. Comput. Phys. 160 (1), 1–28.

Edwards, M.G., 2002. Unstructured, control-volume distributed, full-tensor finite-volume schemes with flow based grids. Comput. Geosci. 6 (3), 433–452.

Fanchi, J., 1983. Multidimensional numerical dispersion. SPE J. 23 (1), 143–151.

Haajizadeh, M., Fayers, F., Cockin, A., Roffey, M., Bond, D., 1999. On the importance of dispersion and heterogeneity in the compositional simulation of miscible gas processes. In: Proceedings of the SPE Asia Pacific Improved Oil Recovery Conference.

Lake, L.W., 1989. Enhanced oil recovery, Prentice Hall, Englewood Cliffs, New Jersey.

Lim, M.T., Pope, G.A., Sepehrnoori, K., Soni, Y., 1997. Grid refinement study of a hydrocarbon miscible gas injection reservoir. In: Paper SPE 38060, Presented at the SPE Asia Pacific Oil and Gas Conference. Kuala Lumpur, Malaysia, April.

Maliska, C.R., 2004. Heat Transfer and Computational Fluid Mechanics, 2nd ed. Editora LTC, Rio de Janeiro, RJ, Brazil.

Marcondes, F., Santos, L.O.S., Varavei, A., Sepehrnoori, K., A 3D hybrid element-based finite-volume method for heterogeneous and anisotropic compositional reservoir simulation. J. Pet. Sci. Eng., (submitted for publication).

Marcondes, F., Sepehrnoori, K., 2007. Unstructured grids and an element based conservative approach for compositional reservoir simulation. In: Proceedings of the 19th International Congress of Mechanical Engineering.

Marcondes, F., Sepehrnoori, K., 2010. An element-based finite-volume method approach for heterogeneous and anisotropic compositional reservoir simulation. J. Pet. Sci. Eng. 73 (1), 99–106.

Oldenburg, C.M., Pruess, K., Benson, S.M., 2001. Process modeling of CO_2 injection into natural gas reservoirs for carbon sequestration and enhanced gas recovery. Energy Fuels 15, 293–298.

Paraschiv, C., Abdev, J., Clemens, T., 2012. Condensate recovery from a fractured carbonate field. In: Paper SPE 153349, Paper Presented at the EAGE Annual Conference & Exhibition Incorporating SPE Europec, 4–7 June. Copenhagen, Denmark.

Parashar, M., Wheeler, J., Pope, G., Wang, K., Wang, P., 1997. A new generation EOS compositional reservoir simulator: part II—framework and multiprocessing. In: Proceedings of the Paper SPE – 37977-MS – SPE Reservoir Simulation Symposium.

Shrivastava, V., Nghiem, L., Moore, R., 2002. A novel approach for incorporating physical dispersion in miscible displacement. In: Proceedings of the SPE Annual Technical Conference and Exhibition.

Shrivastava, V., Nghiem, L., Moore, R., Okazawa, T., 2005a. Modelling physical dispersion in miscible displacement—part 1: theory and the proposed numerical scheme. J. Can. Pet. Technol. 44 (5), 25–33.

Shrivastava, V., Nghiem, L., Moore, R., Okazawa, T., 2005b. Modelling physical dispersion in miscible displacement—part 2: validation, numerical tests, and applications. J. Can. Pet. Technol. 44 (5), 34–43.

Solano, R., Johns, R., Lake, L., 2001. Impact of reservoir mixing on recovery in enriched-gas drives above the minimum miscibility enrichment. SPE Reserv. Eval. Eng. 4 (5), 358–365.

Stalkup, F., 1990. Effect of gas enrichment and numerical dispersion on enriched-gas-drive predictions. SPE Reserv. Eng. 5 (4), 647–655.

Verma, S., Aziz, K., 1997. A control volume scheme for flexible grids in reservoir simulation. In: Proceedings of the Paper SPE 37999, SPE Symposium on Reservoir Simulation.

Wang, P., Wheeler, M., Parashar, M., Sepehrnoori, K., 1997. A new generation EOS compositional reservoir simulator: part I—formulation and discretization. In: Proceedings of the paper SPE 37979, SPE Reservoir Simulation Symposium. Dallas–TX.

Yanze, Y., Clemens, T., 2012. The role of diffusion for nonequilibrium gas injection into a fractured reservoir. SPE Reserv. Eval. Eng. 15, 60–71.